THE JOURNAL OF PHYSICAL CHEMISTRY C
A JOURNAL OF THE AMERICAN CHEMICAL SOCIETY

pubs.acs.org/JPCC

Article

Discovery of Superconductivity in Mercury Cadmium Telluride

Ya-Kang Peng, Feng-Xian Bai, Ge Huang, Hao Yu, Zuo-Yuan Dong, Quan-Zhi Sun, Ning Dai, Yan Sun,* and Xiao-Jia Chen*

Cite This: J. Phys. Chem. C 2021, 125, 24746−24754

Read Online

ACCESS | Metrics & More | Article Recommendations

ABSTRACT: Mercury cadmium telluride compounds exhibit large tunability of nontrivial electronic states by modifying chemical composition, temperature, or pressure. Despite the growing interest in $Hg_{1-x}Cd_xTe$, very little information currently exists on how their electrical properties are affected upon compression. Here, we systematically investigate the high-pressure behaviors of bulk Au-doped $Hg_{0.781}Cd_{0.219}Te$ crystals with the doping level close to the Kane fermion point. A clear structure evolution path of this compound with pressure varying from zinc blende ($F4\bar{3}m$) through cinnabar ($P3_121$) and rocksalt ($Fm\bar{3}m$) to the orthorhombic one ($Cmcm$) is established from the measurements of phonon spectra, resistivity, and the Hall effect. Pressure-induced phonon softening is proposed to be the driving force for the phase transition. The last two phases are found to exhibit superconductivity with different pressure dependence of the critical temperature. These results and findings suggest that superconductivity is the general nature of mercury cadmium tellurium compounds at high pressures. The group II−VI compounds thus also offer a pool for finding new superconductors.

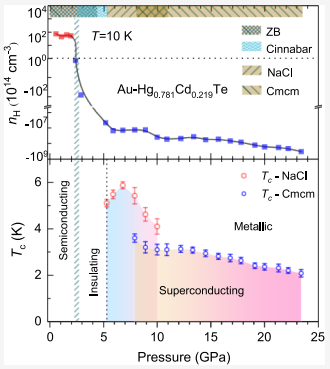

INTRODUCTION

The binary and ternary compounds within the group II−VI family have been widely used in optoelectronic detectors and phase-change memory devices.[1,2] Among them, mercury cadmium telluride (MCT) compounds, the alloys of HgTe and CdTe, are the most attractive for their unique physical properties. $Hg_{1-x}Cd_xTe$ forms a continuous series of solid solutions over the whole composition range x while keeping the zinc blend (ZB) crystalline structure and the lattice parameters virtually unaltered.[3] Accordingly, the MCT alloys exhibit a large energy gap tunability with the band gap ranging from the normal band ordering with $E_g = E_6 - E_8 = 1.6$ eV for CdTe to the inverted band ordering with $E_g = E_6 - E_8 = -0.30$ eV for HgTe at 4.2 K.[1] Based on the concept of band inversion, multiple topological nontrivial phases, such as 2D topological insulators and 3D Weyl semimetals, have been predicted or confirmed in strained HgTe thin films[4−8] and narrow- or negative-band gap MCT compounds[9] and their analogues.[8] More intriguingly, the HgTe-based compounds possess enormous potential in achieving the long-sought ideal Weyl semimetal,[7,9] providing a great platform to study the spectacular transport properties due to the chiral anomaly, such as negative magnetoresistance[10,11] and chiral magnetic effects.[10−12] Subsequently, another massless quasiparticle, the so-called Kane fermion, is observed in $Hg_{1-x}Cd_xTe$ with $x \approx 0.17$ at 77 K, in which the vertex of the s-type Γ_6 and the p-type Γ_8 bands overlap each other at the Γ point of the first Brillouin zone with an additional flat band.[13,14] However, a fine tuning of the band gap of $Hg_{1-x}Cd_xTe$ crystals *via* the variation in the chemical composition x is not allowed due to the inherent fluctuations of Hg concentration with the standard sequence of different symmetry bands.

Pressure has been shown to be an effective method to modify the crystal structure and the corresponding electronic states.[15−19] Extensive theoretical calculations suggest that the chemical bonds in MCT compounds are sensitive to the external pressure or strain.[5−8] By effectively shortening the atomic spacing along the [001] direction to remove the time-reversal symmetry, it is possible to achieve the mutual electronic phase transformation between a normal insulator, topological insulator, and Weyl semimetal in a wide composition range around the Kane fermion point ($0.1 \leq x \leq 0.25$).[9] Thus, the investigation of the pressure-induced topological transitions and superconductivity of MCT compounds is of big interest. In the past decades, numerous studies focused on investigating the pressure-induced phase transition of HgTe-based materials. The structure evolution with pressure of powdery HgTe[21] and $Hg_{0.8}Cd_{0.2}Te$[26] has been well characterized by both synchrotron X-ray diffraction (XRD) and room-temperature resistance measurements, namely, from the semiconducting or semimetallic ZB phase with the space group $F4\bar{3}m$ to the metallic rocksalt ($Fm\bar{3}m$) phase followed by another phase transition to the metallic

Received: September 16, 2021
Revised: October 19, 2021
Published: November 2, 2021

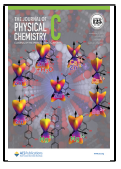

https://doi.org/10.1021/acs.jpcc.1c08169
J. Phys. Chem. C 2021, 125, 24746−24754

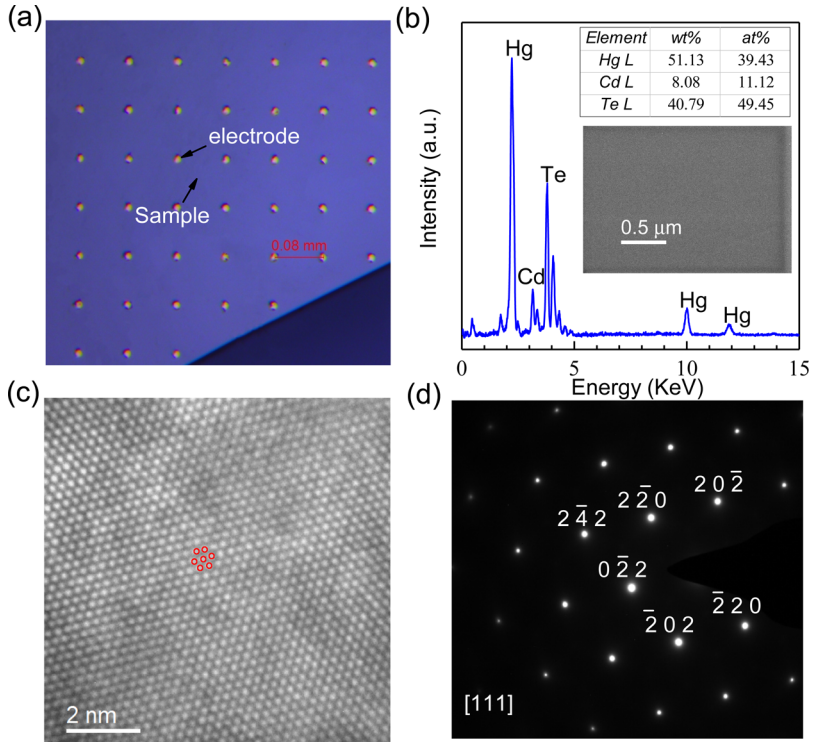

Figure 1. Structure and characterization of the Au-doped $Hg_{0.781}Cd_{0.219}Te$ single crystal. (a) Optical image of the produced $Hg_{0.781}Cd_{0.219}Te$ crystal after the photolithography process. (b) Typical energy-dispersive spectroscopy data and the corresponding scanning electron microscopy image. The transmission electron microscopy image (c) and selected area electron diffraction pattern (d) for the grown $Hg_{0.781}Cd_{0.219}Te$ crystal.

orthorhombic *Cmcm* phase.[20−27] In particular, an insulator-like cinnabar ($P3_121$) structure appears between the ZB and rocksalt at relatively low pressures.[20,21,26,27] Minimizing the electrical contact resistance between the contact material and MCT compounds is still a challenge at high pressures. There is still lack of the comprehensive understanding of the evolution of chemical bonds and electrical transport behaviors with pressure in the view of experiment. Moreover, the strained HgTe films have been widely used to investigate the proximity effect where a topological insulator comes in contact with a superconductor.[28−31] However, to our knowledge, the superconductivity or even topological superconductivity of the bulk MCT compounds at high pressures has not been explored up to now.

With increasing *x*, the pressure-induced ZB to cinnabar phase transition of MCT compounds shifts from 1.3 to 3.5 GPa.[20,21] To maintain the ZB phase over a relatively wide pressure range, we choose the Au-doped $Hg_{0.781}Cd_{0.219}Te$ as the prototype system. The band gap of undoped $Hg_{0.781}Cd_{0.219}Te$ is around 0.11 eV at 10 K. The doping of Au further decreases the energy gap to a value closed to the Kane fermion point.[32] Moreover, the Au-doped $Hg_{0.781}Cd_{0.219}Te$ is around the most widely used mole fraction of p-type MCT in infrared technology.[33,34]

In this work, the abovementioned issues are addressed by combining the *in situ* Raman scattering, resistivity, and Hall effect measurements on Au-doped $Hg_{0.781}Cd_{0.219}Te$ crystals under pressure. Upon compression, the electrical transport measurements reveal that the system undergoes a semiconductor−insulator−metal transition, which is associated with the phase transformation from the ZB ($F4\bar{3}m$) through cinnabar ($P3_121$) to rocksalt ($Fm\bar{3}m$). More interestingly, a superconducting state emerges in the metallic rocksalt phase, and the critical temperature (T_c) exhibits a dome-shaped feature with a maximum value of 5.9 K at 6.8 GPa. At higher pressure, another phase transition to *Cmcm* occurs at 7.9 GPa while the system remains superconducting with the T_c value around 3 K.

MATERIALS AND METHODS

The Au-doped $Hg_{0.781}Cd_{0.219}Te$ crystal was grown on the lattice-matched (111)B CdZnTe substrate in Te-rich solution by the vertical liquid-phase epitaxy method at 733 K. High purity mercury, cadmium, and telluride raw materials (99.99999 wt % purity) were used as the solution of LPE. The composition of $Hg_{0.781}Cd_{0.219}Te$ was determined by both Fourier transform infrared spectroscopy and scanning electron microscopy with energy-dispersive spectroscopy. The doping concentration of Au measured by secondary-ion mass spectrometry[34] is around 1.5×10^{16} cm^{-3}. The prepared samples were studied by transmission electron microscopy (FEI Tecnai G2F20) and the corresponding selected area electron diffraction (FEI Talos F200X). To reduce the contact resistance, we fabricated circular indium electrodes with a diameter of 5 μm on the surface of the sample by adopting micron lithography technique. The distance between the nearest neighbor electrodes is 80 μm. The crystals were then thinned mechanically down to flakes of 35 μm.

Pressure- and temperature-dependent electrical transport and Hall resistivity measurements were conducted using a quasi-four-probe method in the quantum designáŕs physical property measurement system. A miniature diamond anvil cell with anvils of 500 μm culet is used for the electrical and Hall effects measurements. The applied magnetic flied is perpendicular to the current direction. A cubic boron nitride layer was chosen as an electric insulator between electrode leads and the

https://doi.org/10.1021/acs.jpcc.1c08169
J. Phys. Chem. C 2021, 125, 24746−24754

Re gasket. A micron mechanically exfoliated sample with size 80 × 80 × 35 μm^3 with four Pt wires adhered to it using silver epoxy was placed in the sample chamber with Daphne oil 7373 as pressure-transmitting medium to maintain the hydrostatic pressure environment. For the Raman measurements, a Mao–Bell diamond anvil cell with anvils of 500 μm culet and Re gasket is used. Neon was loaded as the pressure transmitting medium. The Raman spectra were measured using a single-stage spectrograph equipped with an array thermoelectrically cooled charge-coupled device detector. The Raman notch filters were of a very narrow bandpass, allowing Raman measurements down to 10 cm^{-1} in Stokes and anti-Stokes. The 488 nm excitation was used to illuminate a circle with a diameter of 5 μm. To avoid potential overheating or oxidation of the sample, we used the highest laser power level of 1 mW. The pressure was determined from the ruby fluorescence shift in all of our experiments.

RESULTS AND DISCUSSION

Prior to physical property measurements, the synthesized MCT samples were structurally characterized using high-resolution scanning electron microscopy and transmission electron microscopy as shown in Figure 1. The scanning electron microscopy image [the inset of Figure 1b] shows a high homogeneity of the crystal. The corresponding energy-dispersive spectroscopy data in Figure 1b gives the atomic ratio of elements Hg/Cd/Te = 39.43:11.12:49.45 without detection of any other impurities. Note that the doping concentration of Au atoms is only at a rate of one in a few million. Hence, there is no signal of the gold in the energy-dispersive spectroscopy data. The atomic arrangement of sample was determined using high-resolution transmission electron microscopy and selected area electron diffraction patterns, as presented in Figure 1c,d. These results indicate the high-quality single crystalline ZB structure of the sample.

Traditionally, the p-type doping of MCT can be achieved with native defects of mercury vacancies, group I and group V elements. Among them, the most commonly used element is gold for its potential in reducing of the leakage current. The Au atoms act as an acceptor and occupy the Hg sites in MCT crystals prepared by the liquid phase epitaxy method.[35] Electrical transport measurements reveal the p-type character of the grown Au-doped $Hg_{0.781}Cd_{0.219}Te$, as will be discussed below.

Figure 2 presents the high-pressure structural phase transition sequence of $Hg_{1-x}Cd_xTe$ compounds that has been well established, namely, from ZB → cinnabar → NaCl → *Cmcm*. At ambient pressure, $Hg_{0.781}Cd_{0.219}Te$ crystallizes in a ZB structure, with the space group $F\bar{4}3m$,[26] as shown in Figure 2a. The ZB phase is characterized by tetrahedra, each with a central ion surrounded in the first coordination shell by four nearest neighbors at the vertices. Nevertheless, the NaCl structure has sixfold transformation. For the ZB structure, the vibration of the lattice at Γ points can be described with a 2*F*2 symmetry. Also, two Raman-active modes comprising longitudinal-optic (LO) and transverse-optic (TO) phonons have been identified experimentally.[36] For $Hg_xCd_{1-x}Te$, the vibrational spectra of ternary solid solution can be described in terms of five basic elemental tetrahedra T_n[37] (n is the number of Cd atoms in the tetrahedron). Thus, T_0 and T_4 configurations correspond to the strictly binary HgTe and CdTe compounds, and T_{1-3} represents the ternary compounds. In our case, when x = 0.219, the T_0 component

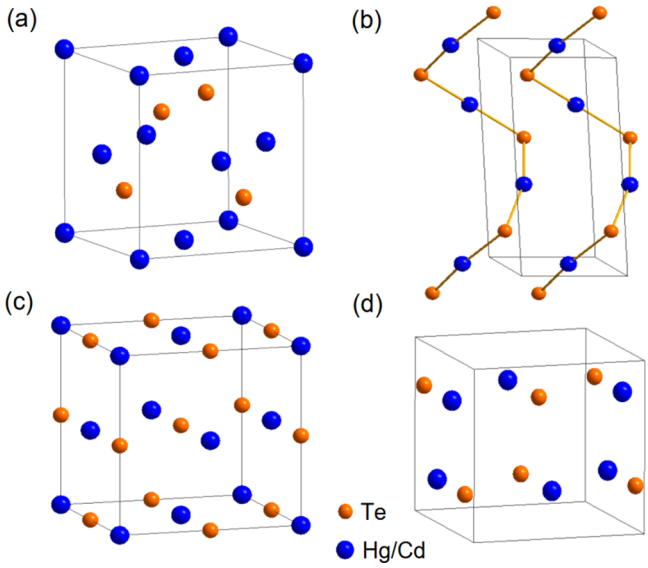

Figure 2. Crystal structures of $Hg_{1-x}Cd_xTe$ at ambient and high pressures, plotted in perspective of using a conventional crystallographic cell. (a) Cubic ZB structure, (b) cinnabar structure, (c) cubic rocksalt structure, and (d) orthorhombic *Cmcm* structure. The blue and orange circles represent Hg/Cd and Te atoms, respectively.

dominates the lattice. Therefore, HgTe-like phonon modes are more pronounced as we observed.

Raman spectroscopy is a widely used and effective method to detect the variety of lattice symmetry. We collected pressure-dependent Raman spectra up to 24.3 GPa as shown in Figure 3. Under ambient conditions, the observed Raman modes of the alloy consist of HgTe- and CdTe-like modes;[36] the former appearing at around 118.3 cm^{-1} (HgTe-like TO) and 139.5 cm^{-1} (HgTe-like LO) labeled TO_1 and LO_1, and the latter occurring at around 163.4 cm^{-1} (a combination of the Cd-like TO an LO) labeled TO_2 + LO_2. The low-frequency D mode is the telluride defect mode as previously reported in some Raman measurements of MCT compunds.[38] Mode softening is found for both HgTe-like LO and TO modes in the pressure range of 0–4 GPa, contrary to the traditional hardening behaviors for a wide-band gap semiconductor, for example, the CdTe-like mode in this work. This softening originates from the weakening of the elastic forces of Hg–Te bonds during compression. Additionally, we notice two new peaks at lower frequency ~35.0 cm^{-1} (M_1) and 161.5 cm^{-1} (M_3) occurring at 2.0 GPa, accompanied by the disappearance of the CdTe-like Raman mode. Upon compression, the TO_1 mode develops a new split-off feature, and it strengthens with pressure up to 4.4 GPa and then suddenly disappears at pressures above 4.9 GPa. At pressures above 8.7 GPa, four Raman modes labeled M_4-M_7 appear gradually. Therefore, our Raman data provide consistent evidence of the previous XRD data for the structural transition.[39] Upon the pressure being released, we observed the co-existing phases and the recovery to the initial phase at ambient pressure.

It is speculated that the mode softening observed in tetrahedrally coordinated compound is responsible for driving the phase transition.[40,41] The mode softening process persists until the Raman modes of the ZB phase totally disappear at 4.4 GPa, and then, the pure Raman spectra of the cinnabar phase can be identified as shown in the middle panel of Figure 3b. Interestingly, slightly changing the external pressure would

https://doi.org/10.1021/acs.jpcc.1c08169
J. Phys. Chem. C 2021, 125, 24746–24754

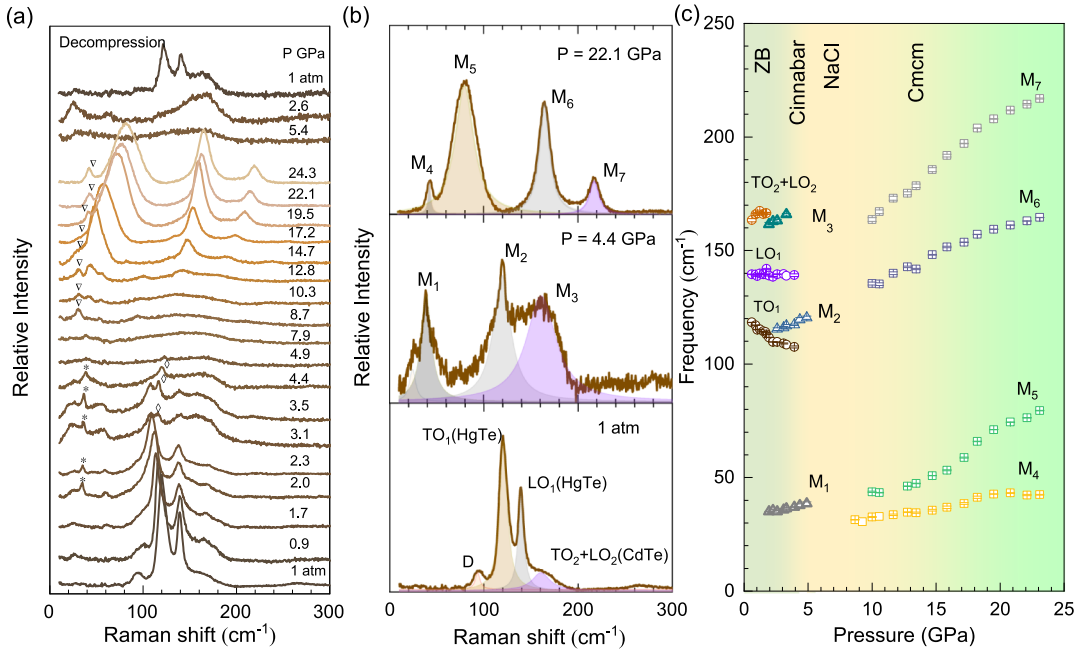

Figure 3. High-pressure Raman spectra of Au-doped $Hg_{0.781}Cd_{0.219}Te$ at room temperature. (a) Raman spectra at various pressures up to 24.3 GPa in the compression run together with the decompression run down to 1 atm. Three phase transitions are clearly observed with strong reversibility in both compression−decompression runs. (b) Upper, middle, and lower panel represents the typical Raman spectra of the *Cmcm*, cinnabar, and ZB phase at each given pressure, respectively. The shadow regions are the fitting curves extracted using multi-Lorentzian functions. (c) Frequencies of phonon modes as a function of pressure. Except the HgTe-like TO_1 and LO_1 modes, all the peaks of the vibration modes shift to higher frequencies as the pressure is increased.

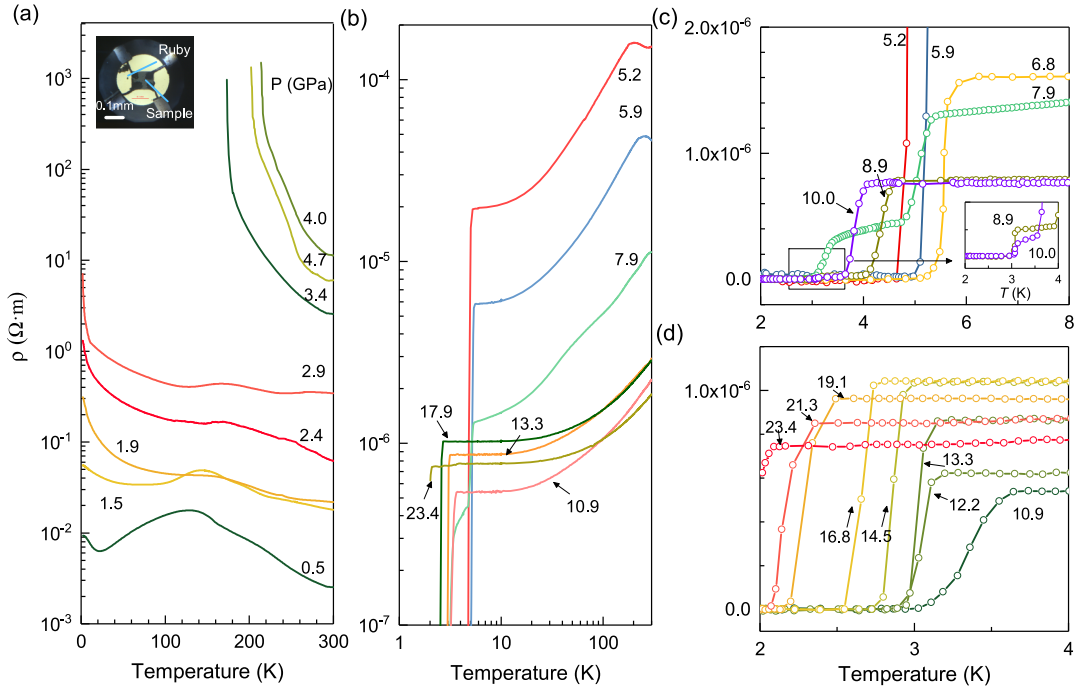

Figure 4. High-pressure electrical transport properties of Au-doped $Hg_{0.781}Cd_{0.219}Te$ up to 23.4 GPa. Temperature-dependent resistivity (ρ) for pressures 0.5−4.7 (a) and 5.2−23.4 GPa (b), respectively. The inset in (a) is a microphotograph of the sample with four Pt electrodes in a diamond anvil cell. Clear resistivity drops as the signature of superconductivity is observed at pressure above 5.2 GPa. (c,d) Enlarged temperature-resistivity curves around the superconducting transitions.

drive the compound to enter the six-coordination rocksalt phase, which would result in the disappearance of all Raman modes. Our findings reveal that the cinnabar phase behaves more like an intermediate phase. It plays an important role in the transformation from the four coordination to six coordination. The pressure dependence of the vibrational frequencies of the observed modes is summarized in Figure 3c. Except the HgTe-like modes, all the Raman peaks are found to shift to higher frequencies with increasing pressure, especially for the M_5−M_7 modes of the *Cmcm* phase.

https://doi.org/10.1021/acs.jpcc.1c08169
J. Phys. Chem. C 2021, 125, 24746−24754

Figure 4 shows the evolution of resistivity as a function of temperature $\rho(T)$ of Au-doped $Hg_{0.781}Cd_{0.219}Te$ at various pressures. Overall, the $\rho(T)$ curves exhibit a typical weak semiconducting behavior with an anomalous hump at relatively low pressures. This anomaly is associated with the conduction-type conversion, which has been widely seen in narrow-band gap MCT compounds.[42] Upon compression, the hump moves toward higher temperature gradually and vanishes at 1.9 GPa. In addition, the intersection of $\rho(T)$ curves at 1.5 and 1.9 GPa is somewhat remarkable. For the region of $2.4 < P < 4.0$ GPa, the resistivity increases sharply (around four orders of magnitude) with the increasing pressure and reaches its maximum value of 10.4 Ω·m at 300 K. The negative slope of temperature dependence of resistance ($dR/dT < 0$) indicates that the compound enters a pure insulating-like phase.

Upon compression, the room-temperature resistivity exhibits an abrupt drop about five orders of magnitude, as shown in Figure 4b. Such an insulator−metal transition is corroborated with the structural transformation from cinnabar to NaCl. At 5.2 GPa, a sudden drop in resistivity appears in the $\rho(T)$ curve at temperatures below 5.1 K, which is the signature of the superconducting transition. As pressure is increased, the transition is seen to shift to higher temperatures, reaching the maximum value at around 5.9 K at 6.8 GPa. The pressure dependence of T_c changes dramatically when the pressure is further increased above 7.9 GPa. As can be seen in Figure 4c, two distinct transitions appear in the resistance versus T curves, signifying the occurrence of the *Cmcm* phase with lower transition temperature. The observed co-existence of these two phases throughout a wide range of pressure indicates a slow kinetics of the structural transformation of the sample, which is additionally aggravated by an inhomogeneous pressure distribution inside the cell. In the pressure range of 10−24 GPa, the T_c shows decrease with $dT_c/dP \sim 0.08$ K/GPa.

In order to confirm the nature of superconductivity, we conducted the resistivity measurements in the vicinity of T_c in different magnetic fields at 5.2 and 13.4 GPa, which correspond to the stable NaCl and *Cmcm* phase, respectively. As can be seen from Figure 5a,b, the T_c is suppressed gradually with increasing magnetic filed. Fitting the experimental data by using the Ginzburg−Landau (GL) formula[45]

$$H_{c2}(T) = H_{c2}(0)\frac{1-(T/T_c)^2}{1+(T/T_c)^2} \tag{1}$$

we estimated the upper critical fields at $T = 0$ K to be 5.58 T at 5.2 GPa and 0.68 T at 13.4 GPa, which are within the Pauli limit of $H_{c2}(T) = 1.84T_c$ for a superconductor with an isotropic SC gap and zero spin−orbital coupling. From the GL formula $H_{c2}(0) = \Phi_0/2\pi\xi(0)^2$, where the Φ_0 is fluxoid and $\xi(0)$ is the coherence length at zero temperature, we can obtain the $\xi(0)$ with a value of 2.6 nm at 5.2 GPa and 0.9 nm at 13.4 GPa, respectively. It is emphasized that the $H_{c2}(0)$ of the NaCl phase is nearly one order of magnitude higher than that of *Cmcm* phase. Such a big difference may be associated with the different superconducting pairing mechanisms of these two phases, which need to be further classified.

Figure 6 displays the Hall electrical conductivity σ_{xy} as a function of the applied magnetic field at a temperature of 10 K and various pressures. At low pressures, σ_{xy} exhibits a nonlinear feature in high magnetic fields, revealing the co-existence of the electrons and holes. Upon compression, the electrons become predominant in the electrical transport, and thus both σ_{xy} and

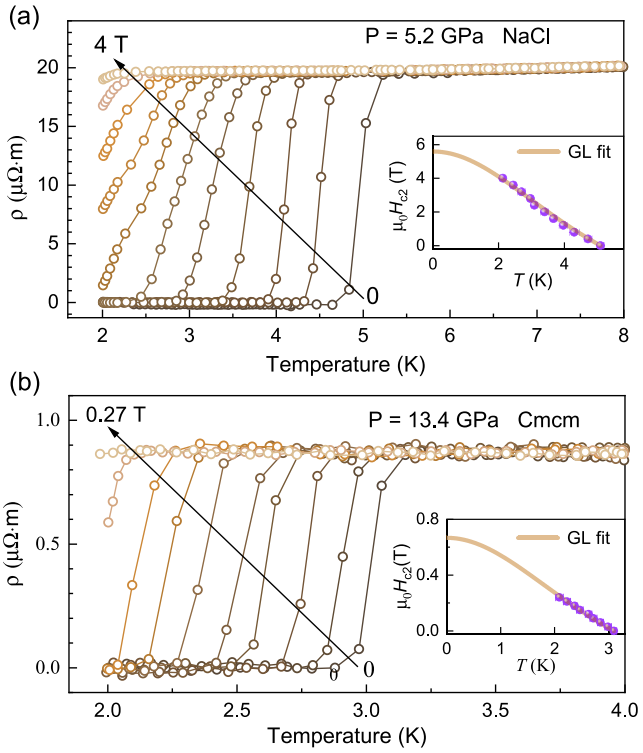

Figure 5. Determination of the value of the upper critical field (H_{c2}) for the superconductor $Hg_{0.781}Cd_{0.219}Te$. Temperature dependence of electrical resistivity at a pressure of 5.2 GPa in the NaCl phase (a) and 13.4 GPa in the *Cmcm* phase (b) in different magnetic fields. The inset shows plot of H_{c2} as a function of temperature. The solid lines represent the GL fitting results to the experimental data points.

its slope are shown to change their signs at pressures above 2.4 GPa. Therefore, we can extract the carrier density n_i (i = h and e) and mobility μ_i (i = h and e) at 0.5, 1.5, 1.9, and 2.4 GPa within the semiclassical two-band Drude model[44]

$$\sigma_{xy}(H) = \frac{\rho_{xy}(H)}{\rho_{xx}^2(H) + \rho_{xy}^2(H)} = \left[\frac{n_h\mu_h^2}{1+(\mu_h H)^2} - \frac{n_e\mu_e^2}{1+(\mu_e H)^2}\right]eH \tag{2}$$

where n_h (n_e) denotes the carrier density of holes (electrons) and μ_h (μ_e) denotes the mobility of holes (electrons). The fitted results with curves are presented in Figure 6. For pressures above 2.9 GPa, the Hall conductivity tends to be linear. Thus, we assume the n_h to be zero, at which the two-band model degenerates to the single-band model. For clarity, we calculated the effective carrier density n_H according to the following equation

$$n_H = \frac{(n_h\mu_h + n_e\mu_e)^2}{n_h\mu_h^2 - n_e\mu_e^2} \tag{3}$$

As plotted in the upper panel of Figure 7, n_H decreases with pressure slightly in the pressure range of 0.5−1.9 GPa, thus giving rise to an increase in resistivity during compression. The decreased n_H implies that the band gap of Au-doped $Hg_{0.781}Cd_{0.219}Te$ increases on applying pressure, which is clearly distinguished from the theoretical calculations based on the simple $\vec{k}\cdot\vec{p}$ model.[9,43]

https://doi.org/10.1021/acs.jpcc.1c08169
J. Phys. Chem. C 2021, 125, 24746−24754

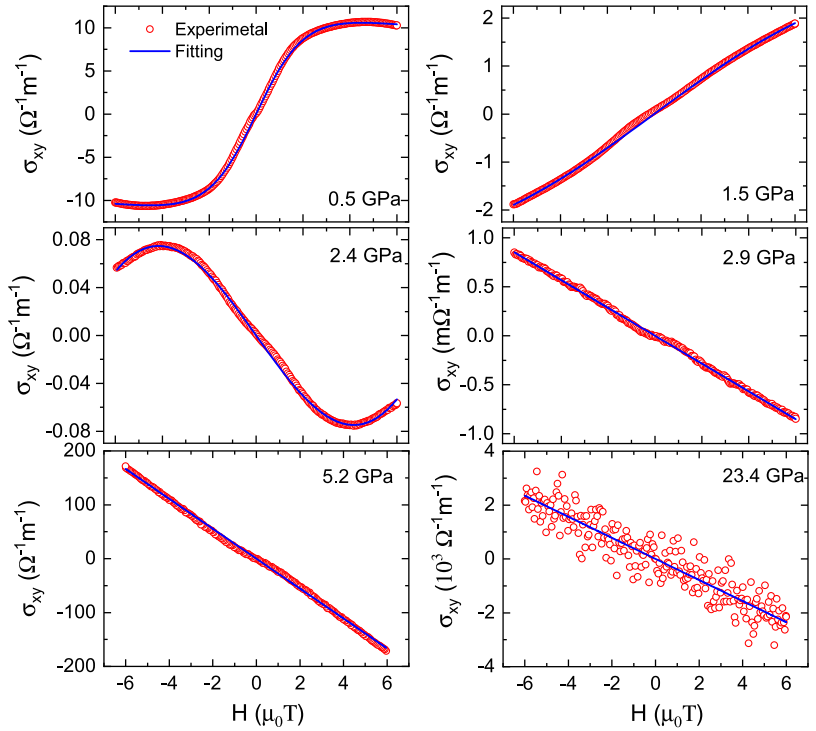

Figure 6. Hall electrical conductivity σ_{xy} as a function of the magnetic field of the Au-doped $Hg_{0.781}Cd_{0.219}Te$ at various pressures up to 23.4 GPa. The open circles and the dotted lines represent the measured data and the fitting results with the two-carrier mode, respectively.

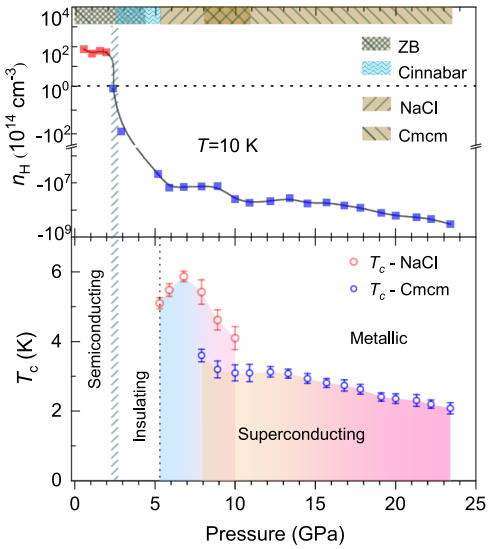

Figure 7. Phase diagram of $Hg_{0.781}Cd_{0.219}Te$ at high pressures. The upper panel shows the plot of the carrier density n_H as a function of pressure measured at 10 K, displaying a sign change from the positive to negative at the critical pressure of 2.4 GPa. The lower panel represents the multiple electronic phases, with the T_c value in open circle.

Upon compression, the effective carrier concentration experiences a minimum with $nH \sim 10^{14}$ cm^{-3} at critical pressure around 2.4 GPa accompanied by a sign change from positive to negative, as shown in the upper panel of Figure 7. Combining these findings with our Raman data and previous XRD data,[26] we reasonably attribute such a semiconducting−insulating transition to the formation of an inhomogeneous mixture of the ZB and cinnabar phase. Upon further compression, there is a seven-order magnitude increase in n_H from 2.4 to 5.2 GPa while the variation of n_H flattens in the pressure range of 5.9−8.9 GPa. Subsequently, the n_H increases slightly with the increase in pressure. Such large change in n_H is associated with the structure transformation from the cinnabar through NaCl to *Cmcm*.

The phase diagram of Au-doped $Hg_{0.781}Cd_{0.219}Te$ is mapped by combining the Raman scattering, resistivity, and Hall effect measurements, as shown in Figure 7. At high pressures, a change in the structure of ZB-$Hg_{0.781}Cd_{0.219}Te$ was observed, forming the ZB and cinnabar mixed phase at 2 GPa and eventually the insulating cinnabar phase at 4.4 GPa. In the ZB-cinnabar phase transition process, the Hall conductivity changes its sign from the positive to negative. Furthermore, compression drives the compounds to enter the metallic rocksalt and *Cmcm* phase in a certain sequence. Both these metallic phases are found to be superconducting with different critical temperatures. We therefore detailed the structural (upper panel) and electronic (lower panel) phase diagrams into four regions in Figure 7.

The onset of the pressure-induced superconductivity was usually associated with the structural transition. The rearrangement of atoms would reconstitute the electronic and vibrational properties where the coupling between electrons and phonons can take place. In BCS theory and the Mcmillan−Allen−Dynes formula,[46,47] the superconductivity originates from the formation of the cooper pairs when the electron−phonon coupling (λ) is strong enough to overcome the Coulomb repulsion. The strength of the electron-phonon coupling is related to the structure of the material, and thus given using the following equation[48]

$$\lambda = \frac{N(E_F)\langle I^2\rangle}{M\omega_p^2} \quad (4)$$

https://doi.org/10.1021/acs.jpcc.1c08169
J. Phys. Chem. C 2021, 125, 24746−24754

where $N(E_F)$ is the electron density of state at the Fermi level, $\langle I^2 \rangle$ is the mean-square electron−ion interaction matrix element, and M and ω_p are the effective atomic mass and phonon frequency, respectively. Thus, T_c can be enhanced by either an increase in the carrier density or the phonon softening. It is worth emphasizing that the increased T_c at 5.2−6.8 GPa is accompanied by the disappearance of the Raman peaks of the cinnabar phase and the increase in the carrier density n_H. The T_c behavior is related to the enhanced crystallinity of the NaCl phase. In the pressure range of 6.8−8.9 GPa, the variation in carrier concentration flattens, while T_c changes its pressure dependence and decreases obviously with increasing pressure. Meanwhile, two distinct transitions appear in the resistance versus T curves due to the co-existence of the NaCl and *Cmcm* phase. Both these transitions are seen to shift to lower temperatures, as shown in the lower panel of Figure 7. At higher pressures, although increasing n_H would increase T_c, the hardening phonon modes (as we observed in our Raman data M_5−M_7) weaken or even suppress this increase.[49] It indicates that the pressure effect of T_c is a result of the interplay of pressure-induced electronic stiffness and phonon hardening. Thus, T_c decreases monotonically with increasing pressure.

There have been a number of studies on the proximity-induced topological superconductivity based on the topological feature from HgTe.[28−31] However, the intrinsic bulk superconductivity of HgTe-based compounds is still absent. Our findings reveal that superconductivity in $Hg_{0.781}Cd_{0.219}Te$ can be achieved by the pressure-induced phonon softening accompanied by the phase transformation. Remarkably, nearly all of the binary CdTe and HgTe and ternary $Hg_{1-x}Cd_xTe$ compounds undergo a similar structure phase transition at high pressures. A slight change in the composition does not affect the fundamental properties of the conducting electrons. Thus, one can expect that superconductivity is the general nature of the high-pressure rocksalt and *Cmcm* phases of the MCT compounds. Moreover, similar to the behaviors of MCT compounds, numerous compounds within the group II−VI family, such as ZnTe,[50,51] HgS/HgTeS,[52] and ZnCdTe,[22] have been shown to be metallic at high pressures. The group II−VI compounds thus also offer a pool for finding new superconductors.

CONCLUSIONS

In conclusion, we have investigated the effect of pressure on Au-doped $Hg_{0.781}Cd_{0.219}Te$ crystals through a series of vibrational and electrical transport measurements. Upon compression, a semiconductor−insulator−metal transition is observed. The structural transformation from ZB → cinnabar → NaCl → *Cmcm* accounts for such dramatic changes in the electronic properties. The pressure-induced phonon softening is suggested to be the driving force for the phase transition. Superconductivity emerges in the metallic NaCl and *Cmcm* phase and the superconducting critical temperature exhibits a dome-shaped feature with a maximum value of 5.9 K at 6.8 GPa. Considering the fact that superconductivity occurs in the high-pressure phases of MCT, our results and discoveries open up a new platform for the possible detection of superconductivity in the group II−VI family. Moreover, $Hg_{1-x}Cd_xTe$ compounds are considered to exhibit topological features under biaxial stress. If these features remain stable in the high-pressure NaCl and *Cmcm* phase, MCT may introduce a new pathway for the exploration of topological superconductivity. Both experimental and theoretical efforts are required to investigate the connection between topology and superconductivity in $Hg_{1-x}Cd_xTe$.

AUTHOR INFORMATION

Corresponding Authors

Yan Sun − *State Key Laboratory of Infrared Physics, Shanghai Institute of Technical Physics, Chinese Academy of Sciences, Shanghai 200083, China;* orcid.org/0000-0002-9801-2987; Phone: +86 (0)21 80177044; Email: sunny@mail.sitp.ac.cn; Fax: +86 (0)21 80177064

Xiao-Jia Chen − *Center for High Pressure Science and Technology Advanced Research, Shanghai 201203, China; School of Science, Harbin Institute of Technology, Shenzhen 518055, China;* orcid.org/0000-0003-3921-9424; Email: xjchen@hpstar.ac.cn

Authors

Ya-Kang Peng − *State Key Laboratory of Infrared Physics, Shanghai Institute of Technical Physics, Chinese Academy of Sciences, Shanghai 200083, China; School of Physical Science and Technology, ShanghaiTech University, Shanghai 201210, China; University of Chinese Academy of Science, Beijing 100049, China; Center for High Pressure Science and Technology Advanced Research, Shanghai 201203, China;* orcid.org/0000-0003-0885-5313

Feng-Xian Bai − *Center for High Pressure Science and Technology Advanced Research, Shanghai 201203, China*

Ge Huang − *Center for High Pressure Science and Technology Advanced Research, Shanghai 201203, China*

Hao Yu − *Center for High Pressure Science and Technology Advanced Research, Shanghai 201203, China; School of Science, Harbin Institute of Technology, Shenzhen 518055, China*

Zuo-Yuan Dong − *Center for High Pressure Science and Technology Advanced Research, Shanghai 201203, China*

Quan-Zhi Sun − *State Key Laboratory of Infrared Physics, Shanghai Institute of Technical Physics, Chinese Academy of Sciences, Shanghai 200083, China*

Ning Dai − *State Key Laboratory of Infrared Physics, Shanghai Institute of Technical Physics, Chinese Academy of Sciences, Shanghai 200083, China*

Complete contact information is available at: https://pubs.acs.org/10.1021/acs.jpcc.1c08169

Notes

The authors declare no competing financial interest.

ACKNOWLEDGMENTS

The experiments conducted at HPSTAR were supported by the National Key R&D Program of China (grant no. 2018YFA0305900). The sample preparation at SITP was financially supported by the National Key R&D Program of China (grant no. 2016YFA0202200), the National Natural Science Foundation of China (grant nos 11933006 and 62004206), and the Frontier Science Research Project (Key Programs) of Chinese Academy of Sciences (grant no. QYZDJ-SSW-SLH018). This work at HIT was supported by the Basic Research Program of Shenzhen (grant no. JCYJ20200109112810241) and the Shenzhen Science and Technology Program (grant no. KQTD20200820113045081). This work was financially supported by the National Post-

Doctoral Program for Innovative Talents (grant no. BX2021091).

REFERENCES

(1) Martyniuk, P.; Antoszewski, J.; Martyniuk, M.; Faraone, L.; Rogalski, A. New concepts in infrared photodetector designs. *Appl. Phys. Rev.* **2014**, *1*, 041102.

(2) Koelmans, W. W.; Sebastian, A.; Jonnalagadda, V. P.; Krebs, D.; Dellmann, L.; Eleftheriou, E. Projected phase-change memory devices. *Nat. Commun.* **2015**, *6*, 8181.

(3) Nimtz, G.; Schlicht, B. *Narrow-Gap Lead Salts*; Springer: Berlin, Heidelberg, 1983.

(4) Bernevig, B. A.; Hughes, T. L.; Zhang, S.-C. Quantum spin Hall effect and topological phase transition in HgTe quantum wells. *Science* **2006**, *314*, 1757−1761.

(5) Krishtopenko, S. S.; Yahniuk, I.; But, D. B.; Gavrilenko, V. I.; Knap, W.; Teppe, F. Pressure-and temperature-driven phase transitions in HgTe quantum wells. *Phys. Rev. B* **2016**, *94*, 245402.

(6) Brüne, C.; Liu, C. X.; Novik, E. G.; Hankiewicz, E. M.; Buhmann, H.; Chen, Y. L.; Qi, X. L.; Shen, Z. X.; Zhang, S. C.; Molenkamp, L. W. Quantum Hall effect from the topological surface states of strained bulk HgTe. *Phys. Rev. Lett.* **2011**, *106*, 126803.

(7) Ruan, J.; Jian, S. K.; Yao, H.; Zhang, H.; Zhang, S. C.; Xing, D. Symmetry-protected ideal Weyl semimetal in HgTe-class materials. *Nat. Commun.* **2015**, *7*, 11136.

(8) Mahler, D. M.; Mayer, J. B.; Leubner, P.; Lunczer, L.; Sante, D. D.; Sangiovanni, G.; Thomale, R.; Hankiewicz, E. M.; Buhmann, H.; Gould, C.; et al. Interplay of Dirac nodes and Volkov-Pankratov surface states in compressively strained HgTe. *Phys. Rev. X* **2019**, *9*, 031034.

(9) Rauch, T.; Achilles, S.; Henk, J.; Mertig, I. Multiple topological nontrivial phases in strained $Hg_xCd_{1-x}Te$. *Phys. Rev. B* **2017**, *96*, 035124.

(10) Nielsen, H. B.; Ninomiya, M. The Adler-Bell-Jackiw anomaly and Weyl fermions in a crystal. *Phys. Rev. B: Condens. Matter Mater. Phys.* **1983**, *130*, 389−396.

(11) Wei, H.; Chao, S.-P.; Aji, V. Excitonic phases from Weyl semimetals. *Phys. Rev. Lett.* **2012**, *109*, 196403.

(12) Son, D. T.; Spivak, B. Z. Chiral anomaly and classical negative magnetoresistance of Weyl metals. *Phys. Rev. B: Condens. Matter Mater. Phys.* **2013**, *88*, 104412.

(13) Orlita, M.; Basko, D. M.; Zholudev, M. S.; Teppe, F.; Knap, W.; Gavrilenko, V. I.; Mikhailov, N. N.; Dvoretskii, S. A.; Neugebauer, P.; Faugeras, C.; et al. Observation of three-dimensional massless Kane fermions in a zinc-blende crystal. *Nat. Phys.* **2014**, *10*, 233−238.

(14) Teppe, F.; Marcinkiewicz, M.; Krishtopenko, S. S.; Ruffenach, S.; Consejo, C.; Kadykov, A. M.; Desrat, W.; But, D.; Knap, W.; Ludwig, J.; et al. Temperature-driven massless Kane fermions in HgCdTe crystals. *Nat. Commun.* **2016**, *7*, 12576.

(15) Gao, L.; Xue, Y. Y.; Chen, F.; Xiong, Q.; Meng, R. L.; Ramirez, D.; Chu, C. W.; Eggert, J. H.; Mao, H. K. Superconductivity up to 164 K in $HgBa_2Ca_{m-1}Cu_mO_{2m+2+\delta}$ (m=1, 2, and 3) under quasihydrostatic pressures. *Phys. Rev. B: Condens. Matter Mater. Phys.* **1994**, *50*, 4260−4263.

(16) Drozdov, A. P.; Eremets, M. I.; Troyan, I. A.; Ksenofontov, V.; Shylin, S. I. Conventional superconductivity at 203 kelvin at high pressures in the sulfur hydride system. *Nature* **2015**, *525*, 73−76.

(17) Somayazulu, M.; Ahart, M.; Mishra, A. K.; Geballe, Z. M.; Baldini, M.; Meng, Y.; Struzhkin, V. V.; Hemley, R. J. Evidence for superconductivity above 260 K in lanthanum superhydride at megabar pressures. *Phys. Rev. Lett.* **2019**, *122*, 027001.

(18) Drozdov, A. P.; Kong, P. P.; Minkov, V. S.; Besedin, S. P.; Kuzovnikov, M. A.; Mozaffari, S.; Balicas, L.; Balakirev, F. F.; Graf, D. E.; et al. Superconductivity at 250 K in lanthanum hydride under high pressures. *Nature* **2019**, *569*, 528−531.

(19) Snider, E.; Dasenbrock-Gammon, N.; McBride, R.; Debessai, M.; Vindana, H.; Vencatasamy, K.; Lawler, K. V.; Salamat, A.; Dias, R. P. Room-temperature superconductivity in a carbonaceous sulfur hydride. *Nature* **2020**, *586*, 373−377.

(20) Nelmes, R. J.; McMahon, M. I.; Wright, N. G.; Allan, D. R. Phase transitions in CdTe to 28 GPa. *Phys. Rev. B: Condens. Matter Mater. Phys.* **1995**, *51*, 15723−15731.

(21) San-Miguel, A.; Wright, N. G.; McMahon, M. I.; Nelmes, R. J. Pressure evolution of the cinnabar phase of HgTe. *Phys. Rev. B: Condens. Matter Mater. Phys.* **1995**, *51*, 8731−8736.

(22) Saqib, H.; Rahman, S.; Errandonea, D.; Susilo, R. A.; Montero, A. J.; Hernandez, P. R.; Munoz, A.; Sun, Y.; Chen, Z. Q.; Dai, N.; et al. Giant conductivity enhancement: Pressure-induced semiconductor-metal phase transition in $Cd_{0.9}Zn_{0.1}Te$. *Phys. Rev. B* **2019**, *99*, 094109.

(23) Radescu, S.; Mujica, A.; Lopez-Solano, J. Theoretical study of pressure-driven phase transitions in HgSe and HgTe. *Phys. Rev. B: Condens. Matter Mater. Phys.* **2011**, *83*, 094107.

(24) Bhalerao, G. M.; Polian, A.; Gauthier, M.; Itié, J.-P.; Baudelet, F.; Ganguli, T.; Deb, S. K.; Mazher, J.; Pagès, O.; Firszt, F.; et al. High pressure x-ray diffraction and extended x-ray absorption fine structure studies on ternary alloy $Zn_{1-x}Be_xSe$. *J. Appl. Phys.* **2010**, *108*, 083533.

(25) Werner, A.; Hochheimer, H. D.; Strössner, K.; Jayaraman, A. High-pressure x-ray diffraction studies on HgTe and HgS to 20 GPa. *Phys. Rev. B: Condens. Matter Mater. Phys.* **1983**, *28*, 3330−3334.

(26) Quadri, S. B.; Skelton, E. F.; Webb, A. W.; Dinan, J. High pressure studies of $Hg_{0.8}Cd_{0.2}Te$. *J. Vac. Sci. Technol., A* **1986**, *4*, 1974−1976.

(27) McMahon, M. I.; Wright, N. G.; Allan, D. R.; Nelmes, R. J. High-pressure crystal structure of HgTe-IV. *Phys. Rev. B: Condens. Matter Mater. Phys.* **1996**, *53*, 2163−2166.

(28) Maire, L.; Oostinga, J. B.; Knott, D.; Biüne, C.; Virtanen, P.; Tkachov, G.; Hankiewicz, E. M.; Gould, C.; Buhamann, H.; Molenkamp, L. W. Induced superconductivity in the three-dimensional topological insulator HgTe. *Phys. Rev. Lett.* **2012**, *109*, 186806.

(29) Hart, S.; Ren, H.; Kosowsky, M.; Ben-Shach, G.; Leubner, P.; Brüne, C.; Buhmann, H.; Molenkamp, L. W.; Halperin, B. I.; Yacoby, A. Controlled finite momentum pairing and spatially varying order parameter in proximitized HgTe quantum wells. *Nat. Phys.* **2017**, *13*, 87−93.

(30) Wiedenmann, J.; Liebhaber, E.; Kübert, J.; Bocquillon, E.; Burset, P.; Ames, C.; Buhmann, H.; Klapwijk, T. M.; Molenkamp, L. W. Transport spectroscopy of induced superconductivity in the three-dimensional topological insulator HgTe. *Phys. Rev. B* **2017**, *96*, 165302.

(31) Hajer, J.; Kessel, M.; Brüne, C.; Stehno, M. P.; Buhmann, H.; Molenkamp, L. W. Proximity-Induced Superconductivity in CdTe-HgTe Core-Shell Nanowires. *Nano Lett.* **2019**, *19*, 4078−4082.

(32) Han, J. L.; Sun, L. Z.; Qu, X. D.; Chen, Y. P.; Zhong, J. X. Electronic properties of the Au impurity in $Hg_{0.75}Cd_{0.25}Te$: First-principles study. *Phys. B* **2009**, *404*, 131−137.

(33) Lei, W.; Antoszewski, J.; Faraone, L. Progress, challenges, and opportunities for HgCdTe infrared materials and detectors. *Appl. Phys. Rev.* **2015**, *2*, 041303.

(34) Shih, H. D.; Kinch, M. A.; Aqariden, F.; Liao, P. K.; Schaake, H. F.; Nathan, V. Development of gold-doped $Hg_{0.79}Cd_{0.21}Te$ for very-long-wavelength infrared detectors. *Appl. Phys. Lett.* **2003**, *82*, 4157−4159.

(35) Sun, Q.; Wei, Y.; Zhang, J.; Sun, R. Effect of Lattice Mismatch on HgCdTe LPE Film Surface Morphology. *J. Electron. Mater.* **2016**, *45*, 4674−4679.

(36) Amirtharaj, P. M.; Tiong, K. K.; Parayanthal, P.; Pollak, F. H.; Furdyna, J. K. Raman characterization of $Hg_{1-x}Cd_xTe$ and related materials. *J. Vac. Sci. Technol., A* **1985**, *3*, 226−232.

(37) Verleur, H. W.; Barker, A. S. Infrared Lattice Vibrations in $GaAs_yP_{1-y}$ Alloys. *Phys. Rev.* **1966**, *149*, 715−729.

(38) Rai, B. K.; Bist, H. D.; Katiyar, R. S.; Chen, K. T.; Burger, A. Controlled micro oxidation of CdTe surface by laser irradiation: A micro-spectroscopic study. *J. Appl. Phys.* **1996**, *80*, 477−481.

(39) Qadri, S. B.; Webb, A. W.; Skelton, E. F.; Moulton, N.; Furdyna, J.; Colombo, L. Effects of Mn on the high pressure phase transtions in HgTe and related materials. *High Pressure Res.* **2012**, *4*, 303−305.

https://doi.org/10.1021/acs.jpcc.1c08169
J. Phys. Chem. C 2021, 125, 24746−24754

(40) Walker, N. J.; Saunders, G. A.; Hawkey, J. E. Soft TA modes and anharmonicity in cadmium telluride. *Philos. Mag.* **1985**, *52*, 1005−1018.
(41) Chen, X.-J. Exploring high-temperature superconductivity in hard matter close to structural instability. *Matter Radiat. Extremes* **2020**, *5*, 068102.
(42) Bogoboyashchyy, V. V.; Izhnin, I. I.; Pociask, M.; Mynbaev, K. D.; Ivanov-Omskiĭ, V. I. Conduction type conversion in ion etching of Au-and Ag-doped narrow-gap HgCdTe single crystal. *Semiconductors* **2007**, *41*, 804−809.
(43) Gilliland, S.; González, J.; Güder, H. S.; Segura, A.; Mora, I.; Muñoz, V. Pressure and temperature dependence of the band-gap in CdTe. *Phys. Status Solidi B* **2003**, *235*, 441−445.
(44) Huang, X.; Zhao, L.; Long, Y. J.; Wang, P. P.; Chen, D.; Yang, Z. H.; Liang, H.; Xue, M. Q.; Weng, H. M.; Fang, Z. Observation of the chiral-anomaly-induced negative magnetoresistance in 3D Weyl semimetal TaAs. *Phys. Rev. X* **2015**, *5*, 031023.
(45) Tinkham, M. *Introduction to Superconductivity*; Kreiger: Malabar, FL, 1980.
(46) Bardeen, J.; Cooper, L. N.; Schrieffer, J. R. Microscopic Theory of Superconductivity. *Phys. Rev.* **1957**, *106*, 162−164.
(47) McMillan, W. L. Transition temperature of strong-coupled superconductors. *Phys. Rev.* **1968**, *167*, 331−344.
(48) Si, C.; Liu, Z.; Duan, W.; Liu, F. First-principles calculations on the effect of doping and biaxial tensile strain on electron-phonon coupling in graphene. *Phys. Rev. Lett.* **2013**, *111*, 196802.
(49) Chen, X.-J.; Struzhkin, V. V.; Kung, S.; Mao, H. K.; Hemley, R. J.; Christensen, A. N. Pressure-induced phonon frequency shifts in transition-metal nitrides. *Phys. Rev. B: Condens. Matter Mater. Phys.* **2004**, *70*, 014501.
(50) Cui, X.; Hu, T.; Yang, J.; Han, Y.; li, Y.; Liu, C.; Wang, Y.; Liu, B.; Ren, W.; Su, N.; et al. The electrical properties of ZnTe under high pressure and moderate temperature. *Phys. Status Solidi C* **2011**, *8*, 1676−1679.
(51) Errandonea, D.; Segura, A.; Martínez-García, D.; Muñoz-San Jose, V. Hall-effect and resistivity measurements in CdTe and ZnTe at high pressure: Electronic structure of impurities in the zinc-blende phase and the semimetallic or metallic character of the high-pressure phases. *Phys. Rev. B: Condens. Matter Mater. Phys.* **2009**, *79*, 125203.
(52) Ponosov, Y. S.; Shchennikov, V. V.; Mogilenskikh, V. E.; Osotov, V. I.; Popova, S. V. Raman spectra and electronic properties of HgTeS crystals at high pressure. *Phys. Status Solidi B* **2001**, *223*, 275−280.

https://doi.org/10.1021/acs.jpcc.1c08169
J. Phys. Chem. C 2021, 125, 24746−24754